INTERNATIONAL JOURNAL FOR NUMERICAL METHODS IN ENGINEERING
Int. J. Numer. Meth. Engng 2004; **59**:197–223 (DOI: 10.1002/nme.868)

An enriched meshless method for non-linear fracture mechanics

B. N. Rao*,† and S. Rahman

Center for Computer-Aided Design, University of Iowa, 208 Engineering Research Facility, Iowa City, IA 52242-1000, U.S.A.

SUMMARY

This paper presents an enriched meshless method for fracture analysis of cracks in homogeneous, isotropic, non-linear-elastic, two-dimensional solids, subject to mode-I loading conditions. The method involves an element-free Galerkin formulation and two new enriched basis functions (Types I and II) to capture the Hutchinson–Rice–Rosengren singularity field in non-linear fracture mechanics. The Type I enriched basis function can be viewed as a generalized enriched basis function, which degenerates to the linear-elastic basis function when the material hardening exponent is unity. The Type II enriched basis function entails further improvements of the Type I basis function by adding trigonometric functions. Four numerical examples are presented to illustrate the proposed method. The boundary layer analysis indicates that the crack-tip field predicted by using the proposed basis functions matches with the theoretical solution very well in the whole region considered, whether for the near-tip asymptotic field or for the far-tip elastic field. Numerical analyses of standard fracture specimens by the proposed meshless method also yield accurate estimates of the J-integral for the applied load intensities and material properties considered. Also, the crack-mouth opening displacement evaluated by the proposed meshless method is in good agreement with finite element results. Furthermore, the meshless results show excellent agreement with the experimental measurements, indicating that the new basis functions are also capable of capturing elastic–plastic deformations at a stress concentration effectively. Copyright © 2003 John Wiley & Sons, Ltd.

KEY WORDS: crack; J-integral; element-free Galerkin method; enriched basis function; non-linear fracture mechanics

1. INTRODUCTION

Since the pioneering work of Irwin [1], who demonstrated that the stress intensity factor (SIF) characterizes linear-elastic crack-tip fields, linear-elastic fracture mechanics (LEFM) methods are now widely used in engineering practice to help ensure that structures fabricated from met-

*Correspondence to: B. N. Rao, Center for Computer-Aided Design, University of Iowa, 208 Engineering Research Facility, Iowa City, IA 52242-1000, U.S.A.
†E-mail: bnrao@engineering.uiowa.edu

Contract/grant sponsor: U.S. National Science Foundation; contract/grant number: CMS-9900196

Received 16 December 2002
Revised 5 March 2003
Accepted 4 May 2003

Copyright © 2003 John Wiley & Sons, Ltd.

als do not fail prematurely. However, in much or all of the working temperature regime of cracked components, such as reactor pressure vessels, automotive structures, micro-electronic devices, aerospace and aircraft propulsion systems, and others, the material is being typically stressed above the brittle-to-ductile transition temperature where the fracture response is essentially ductile and the material is capable of absorbing considerable inelastic deformation. With the knowledge that this energy absorption capability should be exploited so that structural designs based on LEFM methods do not lead to overly large, heavy, and expensive structures, elastic–plastic fracture mechanics (EPFM) methods have evolved and are used in many industries today. This is because the asymptotic solution of the crack-tip field under EPFM conditions, developed by Hutchinson, Rice, and Rosengren (HRR) [2, 3], reveals that the Eshelby–Cherepanov–Rice J-integral [4–6] characterizes the amplitude of this field, just as SIF characterizes the field in LEFM. Therefore, an accurate evaluation of the J-integral and/or other relevant EPFM fracture parameters is essential for simulation-based life-cycle design of engineering structures.

In recent years, various Galerkin-based meshless methods have been developed or investigated to solve fracture mechanics problems without the use of a structured grid [7–16]. These gridless or meshless methods employ moving least-squares (MLS) approximation of a function that permits the resultant shape functions to be constructed entirely in terms of arbitrarily placed nodes. Since no element connectivity data is required, burdensome meshing or remeshing characteristic of the finite element methods (FEM) is avoided. A growing crack can be modelled by simply extending the free surfaces, which correspond to the crack. By sidestepping remeshing requirements, crack-propagation analysis can be significantly simplified. However, most development in meshless methods to date has been focused on only LEFM problems [7–16]. Research in non-linear fracture mechanics using meshless methods has not been widespread and is only currently gaining attention. Recently, Xu and Saigal [17] employed the element-free Galerkin method (EFGM) to study quasi-static crack growth in elastic–plastic materials under plane strain conditions. However, the accuracy of predicted crack-tip fields and J-integral calculations, which are essential for fracture integrity evaluations, were not discussed. Furthermore, the use of enriched basis functions, typically used to capture the LEFM singularity [9], may not be appropriate for solving non-linear fracture mechanics problems. The singularity of crack-tip field in EPFM is different than that in LEFM and depends on the material hardening characteristics. This implies that material properties could be embedded in the development of new or improved basis functions for meshless fracture analysis. Hence, there is a considerable interest in developing meshless methods for solving EPFM problems.

This paper presents an enriched meshless method for fracture analysis of cracks in homogeneous, isotropic, non-linear-elastic, two-dimensional solids, subject to mode-I loading conditions. The method involves an element-free Galerkin formulation and two new enriched basis functions to capture the HRR singularity field in non-linear fracture mechanics. One enriched basis function can be viewed as a generalized enriched basis function, which degenerates to the linear-elastic basis function when the material hardening exponent is unity. The other enriched basis function entails further improvements by adding trigonometric functions. Four numerical examples are presented to illustrate the proposed method. The examples include evaluation of near-tip stress field, J-integral calculations of standard fracture specimens, load vs crack-mouth opening displacement predictions, and comparisons with experimental data.

Copyright © 2003 John Wiley & Sons, Ltd.

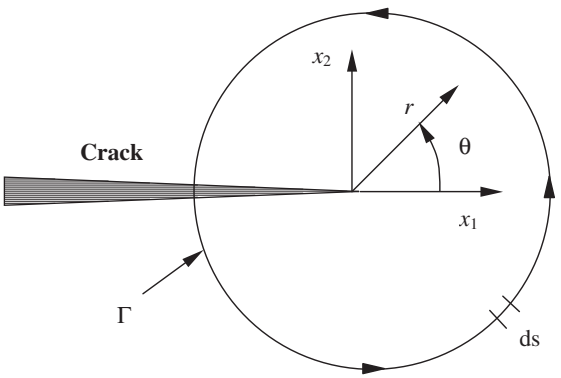

Figure 1. Co-ordinates at the crack tip.

2. THE J INTEGRAL AND HRR FIELD

The J-integral parameter proposed by the Eshelby, Cherepanov, and Rice [4–6] is extensively used in assessing fracture integrity of cracked engineering structures, which undergo plastic deformation at the crack tip. For a general cracked body with an arbitrary counter-clockwise path Γ around the crack tip (see Figure 1), a formal definition of J is

$$J = \int_{\Gamma} \left[W \, \mathrm{d}x_2 - T_i \frac{\partial u_i}{\partial x_i} \, \mathrm{d}s \right] \tag{1}$$

where $W = \int \sigma_{ij} \, \mathrm{d}\varepsilon_{ij}$ is the strain energy density with σ_{ij} and ε_{ij} representing components of stress and strain tensors, respectively, u_i and $T_i = \sigma_{ij} n_j$ are the ith component of displacement and traction vectors, n_j is the j-th component of unit outward normal $\mathbf{n}$ to integration path, and $\mathrm{d}s$ is the differential length along contour Γ.

Consider a power-law hardening material with a uniaxial stress–strain ($\sigma - \varepsilon$) relation as

$$\frac{\varepsilon}{\varepsilon_0} = \alpha \left(\frac{\sigma}{\sigma_0} \right)^n \tag{2}$$

where σ_0 is the reference stress, $\varepsilon_0 = \sigma_0 / E$ is the reference strain with E representing Young's modulus, α is a material constant, and n is the material hardening exponent. When $n = 1$ and ∞, Equation (2) represents linear-elastic and rigid-perfectly plastic materials, respectively. In reality, however, the Ramberg–Osgood law is used to describe non-linear stress–strain curve, which is

$$\frac{\varepsilon}{\varepsilon_0} = \frac{\sigma}{\sigma_0} + \alpha \left(\frac{\sigma}{\sigma_0} \right)^n \tag{3}$$

For multiaxial stress state, the Ramberg–Osgood law can be generalized as

$$\varepsilon_{ij} = \varepsilon_{ij}^{\mathrm{e}}(\sigma_{ij}) + \varepsilon_{ij}^{\mathrm{p}}(\sigma_{ij}) \tag{4}$$

where

$$\varepsilon_{ij}^{\mathrm{e}} = \frac{1+v}{E} s_{ij} + \frac{1-2v}{3E} \sigma_{kk} \delta_{ij} \tag{5}$$

Copyright © 2003 John Wiley & Sons, Ltd.

and

$$\varepsilon_{ij}^{\mathrm{p}} = \frac{3}{2}\,\alpha\varepsilon_0\left(\frac{\sigma_{\mathrm{e}}}{\sigma_0}\right)^{n-1}\frac{s_{ij}}{\sigma_0} \tag{6}$$

are the elastic and plastic components of strain, respectively, v is the Poisson ratio, $s_{ij} = \sigma_{ij} - \sigma_{kk}\delta_{ij}/3$ is the deviatoric stress, $\sigma_{\mathrm{e}} = \sqrt{3s_{ij}s_{ij}/2}$ is the von Mises effective stress, and δ_{ij} is the Kronecker delta. If elastic strains are negligible compared with plastic strains (i.e. $\varepsilon_{ij} \simeq \varepsilon_{ij}^{\mathrm{p}}$), Equation (6) represents a pure power-law-strain-hardening material, for which the asymptotic crack-tip fields under mode-I loading are [2, 3]

$$\sigma_{ij} = \sigma_0\left[\frac{J}{\alpha\sigma_0\varepsilon_0 I_n r}\right]^{1/(n+1)}\tilde{\sigma}_{ij}(\theta, n) \tag{7}$$

$$\varepsilon_{ij} = \alpha\varepsilon_0\left[\frac{J}{\alpha\sigma_0\varepsilon_0 I_n r}\right]^{n/(n+1)}\tilde{\varepsilon}_{ij}(\theta, n) \tag{8}$$

and

$$u_i = \alpha\varepsilon_0 r\left[\frac{J}{\alpha\sigma_0\varepsilon_0 I_n r}\right]^{n/(n+1)}\tilde{u}_i(\theta, n) \tag{9}$$

where r and θ are the polar co-ordinates with the origin at the crack tip, I_n is a dimensionless constant that depends on n, and $\tilde{\sigma}_{ij}$, and $\tilde{\varepsilon}_{ij}$, and $\tilde{u}_i$ are dimensionless angular functions of θ and n. The parameters I_n, $\tilde{\sigma}_{ij}$, $\tilde{\varepsilon}_{ij}$, and $\tilde{u}_i$ also depend on the state of stress. Equations (7)–(9) represent the well-known HRR field under mode-I deformation [2, 3]. Note, the same HRR field also exists in mixed-mode fracture, in which case the dimensionless angular functions also depend on the magnitude of mode-mixity [18].

Although the HRR solution describes the nature of the dominant singularity, higher order terms may have an important effect on the constraint of plane strain crack-tip fields [19–22]. The HRR field is thus not the only possible crack-tip field, but should be regarded as an important limiting case of a family of fields, which arise when higher order terms are insignificant.

3. ENRICHED BASIS FUNCTIONS FOR NON-LINEAR MESHLESS FRACTURE ANALYSIS

There are several ways to enrich the EFGM formulation to capture the stress singularity in fracture analysis. One approach involves augmenting the EFGM trial functions by the near-tip displacement field, thereby including additional unknown coefficients for each crack tip [9]. Hence, both the stiffness matrix and the force vector need to be augmented leading to a larger system of equations. Furthermore, the computer programming can be rather involved. An alternative approach entails expanding the EFGM basis functions directly to include terms from the near-tip displacement field. The enrichment based on expanded basis functions requires simpler computer programming, but can become expensive for multiple cracks [9]. The enrichment based on expanded basis functions was adopted in this study. In this section,

Copyright © 2003 John Wiley & Sons, Ltd.

existing enrichment for LEFM basis functions is briefly summarized and then new enrichment for non-linear fracture mechanics is presented.

3.1. Linear-elastic fracture mechanics

In LEFM, the asymptotic near tip displacement field $\mathbf{u} = \{u_1, u_2\}^{\mathrm{T}}$ is given by

$$u_1 = \frac{1}{\mu}\sqrt{\frac{r}{2\pi}}\,[K_{\mathrm{I}} g_1^{\mathrm{I}}(\theta) + K_{\mathrm{II}} g_1^{\mathrm{II}}(\theta)] \tag{10}$$

and

$$u_2 = \frac{1}{\mu}\sqrt{\frac{r}{2\pi}}\,[K_{\mathrm{I}} g_2^{\mathrm{I}}(\theta) + K_{\mathrm{II}} g_2^{\mathrm{II}}(\theta)] \tag{11}$$

where $\mu = E/[2(1+v)]$ is the shear modulus,

$$\begin{aligned} g_1^{\mathrm{I}}(\theta) &= \kappa - \cos\frac{\theta}{2} + \sin\theta\,\sin\frac{\theta}{2} \\ g_2^{\mathrm{I}}(\theta) &= \kappa + \sin\frac{\theta}{2} - \sin\theta\,\cos\frac{\theta}{2} \\ g_1^{\mathrm{II}}(\theta) &= \kappa + \sin\frac{\theta}{2} + \sin\theta\,\cos\frac{\theta}{2} \\ g_2^{\mathrm{II}}(\theta) &= \kappa - \cos\frac{\theta}{2} - \sin\theta\,\sin\frac{\theta}{2} \end{aligned} \tag{12}$$

are the well-known angular functions of LEFM, K_{I} and K_{II} are mode-I and mode-II SIFs, and the kolosov constant $\kappa = (3-v)/(1+v)$ for plane stress and $\kappa = 3-4v$ for plane stress. Using trigonometric identities, it can be shown that the basis, given by

$$\mathbf{p}^{\mathrm{T}}(\mathbf{x}) = \left\{1, x_1, x_2, \sqrt{r}\cos\frac{\theta}{2}, \sqrt{r}\sin\frac{\theta}{2}, \sqrt{r}\sin\frac{\theta}{2}\sin\theta, \sqrt{r}\cos\frac{\theta}{2}\sin\theta\right\} \tag{13}$$

spans the LEFM crack-tip displacement field in Equations (10) and (11) exactly [9]. Indeed, the enriched basis in Equation (13) has been successfully used in meshless analysis of linear-elastic cracked structures [9, 12–15], including analysis of cracks in functionally graded materials [16]. However, the HRR field is different from the LEFM crack-tip field. Hence, new basis functions need to be developed for non-linear fracture mechanics analysis.

3.2. Non-linear fracture mechanics

According to Equations (7)–(9), the HRR field is a known field. Hence, by embedding the HRR displacement field, enriched basis functions similar to Equation (13) can be developed for its use in non-linear fracture mechanics. However, the angular functions $\tilde{u}_i(\theta, n)$ in Equation (9) cannot be obtained in closed-form. An eigenvalue problem needs to be solved

Copyright © 2003 John Wiley & Sons, Ltd.

numerically to determine $\tilde{u}_i(\theta, n)$ [23]. As an alternative, simpler functional forms that can approximate the HRR field can be potentially used to form the enriched basis.

Consider two approximations of $\tilde{u}_i(\theta, n)$, given by

Approximation I

$$\tilde{u}_i(\theta, n) \simeq \tilde{a}_{0i}(n) + \tilde{a}_{1i}(n) \cos\frac{\theta}{2} + \tilde{a}_{2i}(n) \sin\frac{\theta}{2} + \tilde{a}_{3i}(n) \sin\frac{\theta}{2} \sin\theta + \tilde{a}_{4i}(n) \cos\frac{\theta}{2} \sin\theta \tag{14}$$

and

Approximation II

$$\tilde{u}_i(\theta, n) \simeq \tilde{a}_{0i}(n) + \tilde{a}_{1i}(n) \cos\frac{\theta}{2} + \tilde{a}_{2i}(n) \sin\frac{\theta}{2} + \tilde{a}_{3i}(n) \sin\frac{\theta}{2} \sin\theta + \tilde{a}_{4i}(n) \cos\frac{\theta}{2} \sin\theta + \tilde{a}_{5i}(n) \sin\frac{\theta}{2} \sin 3\theta + \tilde{a}_{6i}(n) \cos\frac{\theta}{2} \sin 3\theta \tag{15}$$

The first equation (Equation (14)) involves a linear combination of components of the basis function vector in Equation (13) (minus the linear terms). The second equation (Equation (15)) entails adding two terms, $\sin(\theta/2)\sin 3\theta$ and $\cos(\theta/2)\sin 3\theta$, to Equation (14) for a better approximation. The selection of the two additional terms, $\sin(\theta/2)\sin 3\theta$ and $\cos(\theta/2)\sin 3\theta$ is made based on a trial and error procedure. Initially the two additional terms were chosen to be, $\sin(\theta/2)\sin 2\theta$ and $\cos(\theta/2)\sin 2\theta$ for a better approximation, but these resulted in ill-conditioned moment matrix (Equation (22)) and subsequent problem in inverting the moment matrix (Equation (22)). Hence, as a second guess the two additional terms were chosen to be $\sin(\theta/2)\sin 3\theta$ and $\cos(\theta/2)\sin 3\theta$, for a better approximation. The latter guess resulted in a well-conditioned matrix, even though the accuracy in the approximation of $\tilde{u}_i(\theta, n)$, using either $\sin(\theta/2)\sin 2\theta$ and $\cos(\theta/2)\sin 2\theta$ or $\sin(\theta/2)\sin 3\theta$ and $\cos(\theta/2)\sin 3\theta$ as additional terms, is observed to be the same. To evaluate both Types I and II approximations, Shih's [23] HRR field data of $\tilde{u}_i(\theta, n)$, $i = 1, 2$, obtained by solving the eigenvalue problem numerically, were fitted with Equations (14) and (15). Note that Shih's [23] HRR field data were reported in polar, co-ordinate system, so a polar to rectangular co-ordinate system transformation was performed before fitting the HRR data using Equations (14) and (15). Figure 2(a) show the plots of $\tilde{u}_i(\theta, n)$ from Equation (14), as a function of θ for materials with high-hardening ($n = 3$), medium-hardening ($n = 10$), and low-hardening ($n = 50$) characteristics for the plane stress condition. The comparison with Shih's HRR field data indicates that Equation (14), obtained from the LEFM basis function, provides a reasonably good approximation of $\tilde{u}_i(\theta, n)$. Similar comparisons in Figure 2(b), which involve plots of Equation (15), show slightly improved results in fitting Shih's numerical results. The above observations also hold true for the plane strain condition, the results of which are shown in Figures 3(a) and 3(b), involving plots of Equations (14) and (15), respectively. Hence, both Equations (14) and (15) can be used to approximate $\tilde{u}_i(\theta, n)$ for

Copyright © 2003 John Wiley & Sons, Ltd.

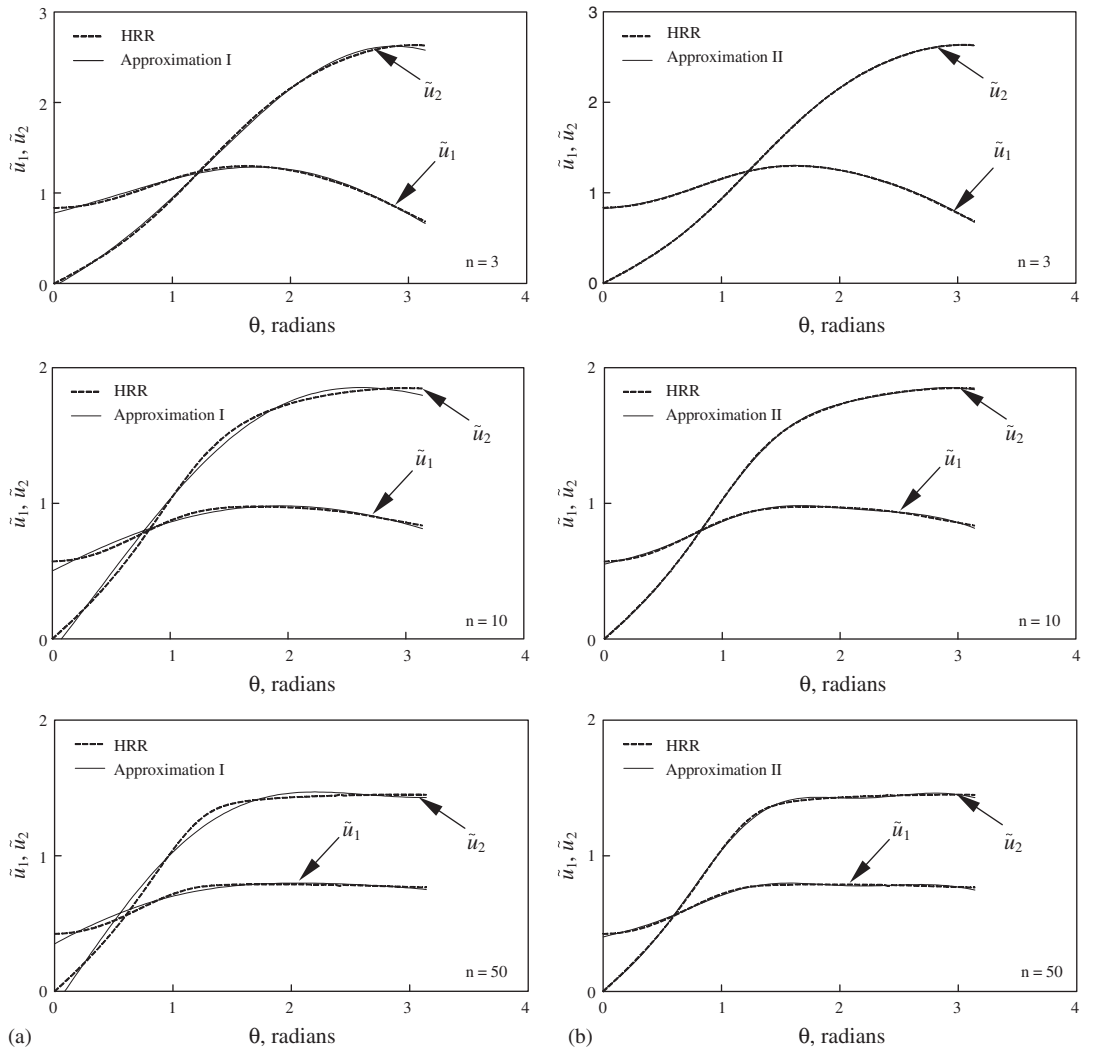

Figure 2. Approximations of HRR displacement field for plane stress: (a) approximation I (Equation (14)); and (b) approximation II (Equation (15)).

non-linear-fracture mechanics analysis. Consequently, two types of enriched basis functions are proposed, which are

$$\text{Type I: } \mathbf{p}^{\mathrm{T}}(\mathbf{x}) = \left\{1, x_1, x_2, r^{1/(n+1)} \cos\frac{\theta}{2}, r^{1/(n+1)} \sin\frac{\theta}{2}, r^{1/(n+1)} \sin\frac{\theta}{2} \sin\theta, r^{1/(n+1)} \cos\frac{\theta}{2} \sin\theta\right\} \tag{16}$$

Copyright © 2003 John Wiley & Sons, Ltd.

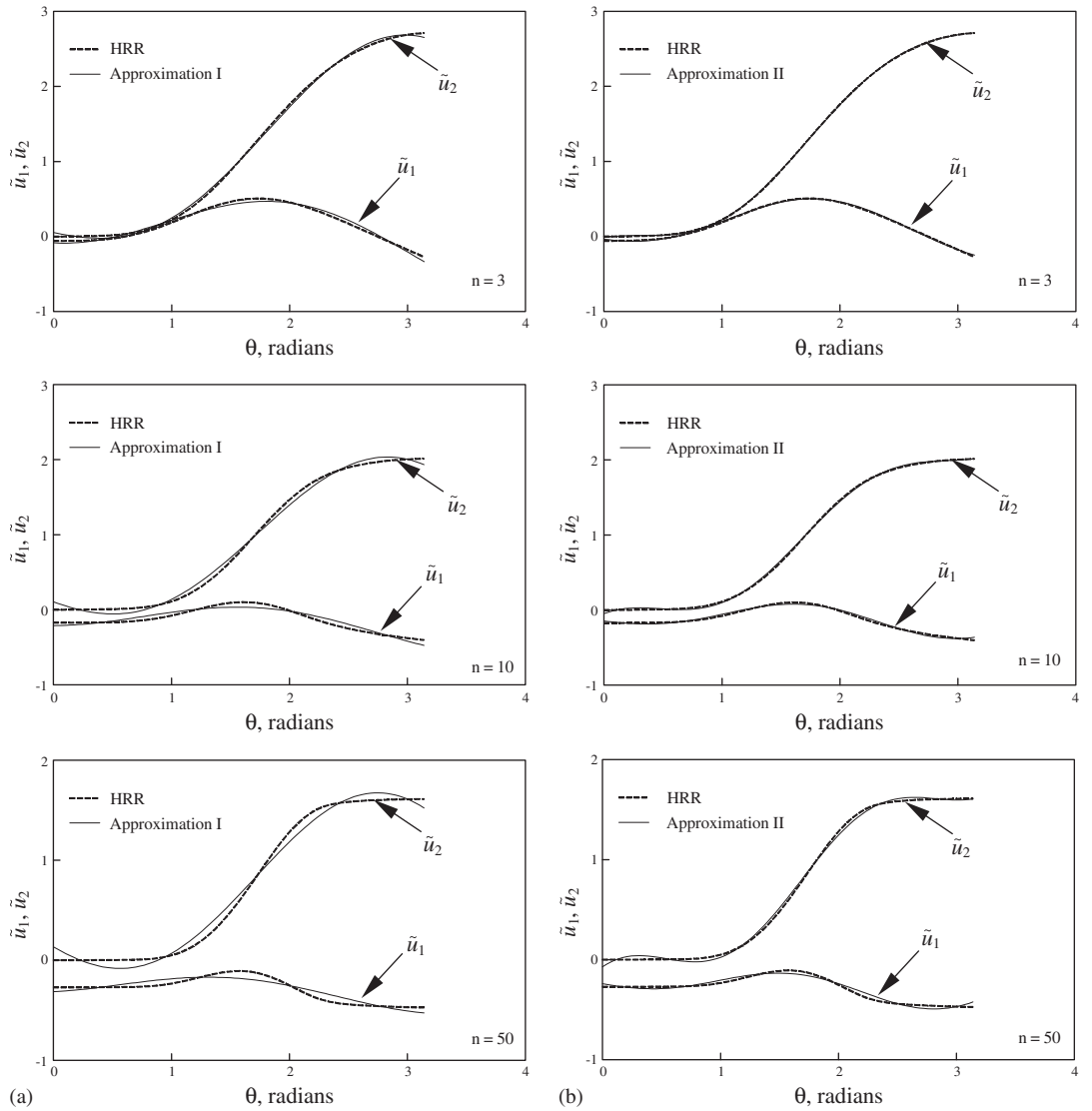

Figure 3. Approximations of HRR displacement field for plane strain: (a) approximation I (Equation (14)); and (b) approximation II (Equation (15)).

and

$$\text{Type II: } \mathbf{p}^{\mathrm{T}}(\mathbf{x}) = \begin{cases} 1, x_1, x_2, r^{1/(n+1)} \cos\dfrac{\theta}{2}, r^{1/(n+1)} \sin\dfrac{\theta}{2}, r^{1/(n+1)} \sin\dfrac{\theta}{2} \sin\theta, r^{1/(n+1)} \cos\dfrac{\theta}{2} \sin\theta, \\ r^{1/(n+1)} \sin\dfrac{\theta}{2} \sin 3\theta, r^{1/(n+1)} \cos\dfrac{\theta}{2} \sin 3\theta \end{cases} \tag{17}$$

Copyright © 2003 John Wiley & Sons, Ltd.

Note, the linear terms in both enriched bases are not related to crack-tip fields, but are needed for linear completeness of EFGM. The Type I enriched basis function in Equation (16) can be viewed as a generalized enriched basis function, which degenerates to the LEFM basis function (Equation (13)) when $n=1$ (linear-elastic).

The dimension of the enriched basis function vector increases when compared with that of commonly used linear or quadratic basis function vectors in solid mechanics. This induces additional computational effort required to invert the moment matrix (Equation (22)) in EFGM. In addition, the enriched basis can also lead to an ill-conditioned moment matrix (Equation (22)). An ill-conditioned moment matrix (Equation (22)) may not affect the quality of meshless solution when the enriched basis is adopted for the entire domain. However, it does have a degrading effect on the quality of meshless solution when coupling shape functions (Equation (28)) from an enriched basis to shape functions from linear or quadratic basis. Two treatments have been found to be effective in alleviating ill-conditioning. One approach involves diagonalizing the EFGM moment matrix (Equation (22)) by Gram–Schmidt orthogonalization. Another approach, which was adopted in this study, entails computing EFGM shape functions using LU decomposition and backsubstitution rather than inverting the moment matrix (Equation (22)). Further details are given by Fleming *et al.* [9].

4. THE ELEMENT-FREE GALERKIN METHOD

4.1. Moving least squares and meshless shape function

Consider a function $u(\mathbf{x})$ over a domain $\Omega \subseteq \Re^2$. Let $\Omega_x \subseteq \Omega$ denote a sub-domain describing the neighbourhood of a point $\mathbf{x} \in \Re^2$ located in Ω. According to the moving least-squares method (MLS) [24], the approximation $u^h(\mathbf{x})$ of $u(\mathbf{x})$ is

$$u^h(\mathbf{x}) = \sum_{i=1}^{m} p_i(\mathbf{x}) a_i(\mathbf{x}) = \mathbf{p}^{\mathrm{T}}(\mathbf{x})\mathbf{a}(\mathbf{x}) \tag{18}$$

where $\mathbf{p}^{\mathrm{T}}(\mathbf{x}) = \{p_1(\mathbf{x}), \ldots, p_m(\mathbf{x})\}$ is a vector of complete basis functions of order m and $\mathbf{a}(\mathbf{x}) = \{a_1(\mathbf{x}), \ldots, a_m(\mathbf{x})\}$ is a vector of unknown parameters that depend on $\mathbf{x}$. The coefficient vector $\mathbf{a}(\mathbf{x})$ is determined by minimizing a weighted discrete $\mathscr{L}_2$ norm, defined as

$$J_E(\mathbf{x}) = \sum_{I=1}^{l} w_I(\mathbf{x})[\mathbf{p}^{\mathrm{T}}(\mathbf{x}_I)\mathbf{a}(\mathbf{x}) - d_I]^2 = [\mathbf{P}\mathbf{a}(\mathbf{x}) - \mathbf{d}]^{\mathrm{T}}\mathbf{W}[\mathbf{P}\mathbf{a}(\mathbf{x}) - \mathbf{d}] \tag{19}$$

where $\mathbf{x}_I$ denotes the co-ordinates of node I, $\mathbf{d}^{\mathrm{T}} = \{d_1, d_2, \ldots, d_n\}$ with d_I representing the nodal parameter for node I, $\mathbf{W} = \mathrm{diag}[w_1(\mathbf{x}), w_2(\mathbf{x}), \ldots, w_l(\mathbf{x})]$ with $w_I(\mathbf{x})$ being the weight function associated with node I, such that $w_I(\mathbf{x}) > 0$ for all $\mathbf{x}$ in the support Ω_x of $w_I(\mathbf{x})$ and *zero* otherwise, l is the number of nodes in Ω_x for which $w_I(\mathbf{x}) > 0$, and $\mathbf{P} = [\mathbf{p}^{\mathrm{T}}(\mathbf{x}_1), \ldots, \mathbf{p}^{\mathrm{T}}(\mathbf{x}_l)] \in \mathscr{L}(\Re^n \times \Re^m)$. In this study, a weight function proposed by Rao and Rahman [12] was used, which is

$$w_I(\mathbf{x}) = \begin{cases} \dfrac{\left(1 + \beta^2 \dfrac{z_I^2}{z_{mI}^2}\right)^{-(1+\beta)/2} - (1+\beta^2)^{-(1+\beta)/2}}{1 - (1+\beta^2)^{-(1+\beta)/2}}, & z_I \leqslant z_{mI} \\ 0, & z_I > z_{mI} \end{cases} \tag{20}$$

Copyright © 2003 John Wiley & Sons, Ltd.

where β is a shape controlling parameter, $z_I = \|\mathbf{x} - \mathbf{x}_I\|$, and z_{mI} is the domain of influence of node I. The stationarity of $J(\mathbf{x})$ with respect to $\mathbf{a}(\mathbf{x})$ yields

$$\mathbf{A}(\mathbf{x})\mathbf{a}(\mathbf{x}) = \mathbf{C}(\mathbf{x})\mathbf{d} \tag{21}$$

where

$$\mathbf{A}(\mathbf{x}) = \sum_{I=1}^{l} w_I(\mathbf{x})\mathbf{p}(\mathbf{x}_I)\mathbf{p}^{\mathrm{T}}(\mathbf{x}_I) = \mathbf{P}^{\mathrm{T}}\mathbf{W}\mathbf{P} \tag{22}$$

and

$$\mathbf{C}(\mathbf{x}) = [w_1(\mathbf{x})\mathbf{p}(\mathbf{x}_1), \ldots, w_l(\mathbf{x})\mathbf{p}(\mathbf{x}_l)] = \mathbf{P}^{\mathrm{T}}\mathbf{W} \tag{23}$$

Solving for $\mathbf{a}(\mathbf{x})$ in Equation (21) and then substituting into Equation (18) yields

$$u^h(\mathbf{x}) = \sum_{I=1}^{l} \Phi_I(\mathbf{x})d_I = \mathbf{\Phi}^{\mathrm{T}}(\mathbf{x})\mathbf{d} \tag{24}$$

where

$$\mathbf{\Phi}^{\mathrm{T}}(\mathbf{x}) = \{\Phi_1(\mathbf{x}), \Phi_2(\mathbf{x}), \ldots \Phi_l(\mathbf{x})\} = \mathbf{p}^{\mathrm{T}}(\mathbf{x})\mathbf{A}^{-1}(\mathbf{x})\mathbf{C}(\mathbf{x}) \tag{25}$$

is a vector with its I-th component,

$$\Phi_I(\mathbf{x}) = \sum_{j=1}^{m} p_j(\mathbf{x})[\mathbf{A}^{-1}(\mathbf{x})\mathbf{C}(\mathbf{x})]_{jI} \tag{26}$$

representing the shape function of the MLS approximation corresponding to node I. The partial derivatives of $\Phi_I(\mathbf{x})$ can also be obtained as

$$\Phi_{I,i}(\mathbf{x}) = \sum_{j=1}^{m} \{p_{j,i}(\mathbf{A}^{-1}\mathbf{C})_{jI} + p_j(\mathbf{A}_{,i}^{-1}\mathbf{C} + \mathbf{A}^{-1}\mathbf{C}_{,i})_{jI}\} \tag{27}$$

where $\mathbf{A}_{,i}^{-1} = -\mathbf{A}^{-1}\mathbf{A}_{,i}\mathbf{A}^{-1}$ and $(\,)_{,i} = \partial(\,)/\partial x_i$.

Note that the MLS/meshless shape function $\Phi_I(\mathbf{x})$ strongly depends on the type of basis functions used. For problem involving cracks, the enriched basis function, such as the one in Equations (16) or (17), is required to produce stress singularity at the crack tip. However, this singularity field is only local to the crack tip. Therefore, it is unnecessary to use an enriched basis for the entire domain. In that case, a hybrid approach involving an enriched basis close to the crack tip and a linear basis function far away from the crack tip can be used. For example, if $\Phi_I^r(\mathbf{x})$ and $\Phi_I^e(\mathbf{x})$ denote two resulting shape functions using regular and enriched basis functions, respectively, the effective shape function due to coupling can be expressed by [9, 12]

$$\Phi_I(\mathbf{x}) = R\Phi_I^e(\mathbf{x}) + (1 - R)\Phi_I^r(\mathbf{x}) \tag{28}$$

where R is an appropriate ramp function that is equal to *unity* on the enriched boundary of the coupling region and *zero* on the regular side of the coupling region. However, in all numerical examples of this study, fully enriched bases are adopted for the entire domain.

Copyright © 2003 John Wiley & Sons, Ltd.

4.2. *Variational formulation and discretization*

For small displacements in two-dimensional, homogeneous, isotropic solids, the equilibrium equations and boundary conditions are

$$\nabla \cdot \sigma + \mathbf{b} = \mathbf{0} \quad \text{in } \Omega \tag{29}$$

and

$$\begin{aligned} &\boldsymbol{\sigma} \cdot \mathbf{n} = \bar{\mathbf{t}} \quad \text{on } \Gamma_t \text{ (natural boundary conditions)} \\ &\mathbf{u} = \bar{\mathbf{u}} \quad \text{on } \Gamma_u \text{ (essential boundary conditions)} \end{aligned} \tag{30}$$

respectively, where $\boldsymbol{\varepsilon}$ is the stress vector, $\boldsymbol{\varepsilon} = \nabla_s \mathbf{u}$ is the strain vector, $\mathbf{u}$ is the displacement vector, $\mathbf{b}$ is the body force vector, $\bar{\mathbf{t}}$ and $\bar{\mathbf{u}}$ are the vectors of prescribed surface tractions and displacements, respectively, $\mathbf{n}$ is a unit normal to the domain, Ω, Γ_t and Γ_u are the portions of boundary Γ where tractions and displacements are prescribed, $\nabla^{\mathrm{T}} = \{\partial/\partial x_1, \partial/\partial x_2\}$ is the vector of gradient operators, and $\nabla_s \mathbf{u}$ is the symmetric part of $\nabla \mathbf{u}$. The variational or weak form of Equations (29) and (30) is

$$\int_\Omega \boldsymbol{\sigma}^{\mathrm{T}} \delta \boldsymbol{\varepsilon} \, \mathrm{d}\Omega - \int_\Omega \mathbf{b}^{\mathrm{T}} \delta \mathbf{u} \, \mathrm{d}\Omega - \int_{\Gamma_t} \mathbf{t}^{\mathrm{T}} \delta \mathbf{u} \, \mathrm{d}\Gamma + \delta W_u = 0 \tag{31}$$

where δ denotes the variational operator and δW_u represents a term introduced to enforce essential boundary conditions. The explicit form of this term depends on the method by which the essential boundary conditions are imposed [17]. In this study, W_u is defined as

$$W_u = \sum_{\mathbf{x}_K \in \Gamma_u} \mathbf{f}^{\mathrm{T}}(\mathbf{x}_K)[\mathbf{u}(\mathbf{x}_K) - \bar{\mathbf{u}}(\mathbf{x}_K)] \tag{32}$$

where $\mathbf{f}^{\mathrm{T}}(\mathbf{x}_K)$ is the vector of reaction forces at the constrained node K on Γ_u. Hence,

$$\delta \mathbf{W}_u = \sum_{\mathbf{x}_K \in \Gamma_u} \delta \mathbf{f}^{\mathrm{T}}(\mathbf{x}_K)[\mathbf{u}(\mathbf{x}_K) - \bar{\mathbf{u}}(\mathbf{x}_K)] + \mathbf{f}^{\mathrm{T}}(\mathbf{x}_K) \delta \mathbf{u}(\mathbf{x}_K) \tag{33}$$

Consider a vector of all prescribed displacements on Γ_u, $\mathbf{g} = \{\bar{\mathbf{u}}(\mathbf{x}_{K_1}), \ldots, \bar{\mathbf{u}}(\mathbf{x}_{K_L})\}^{\mathrm{T}} \in \Re^{2L}$. The variational form given by Equations (31) and (33) can then be expressed by

$$\int_\Omega \boldsymbol{\sigma}^{\mathrm{T}} \delta \boldsymbol{\varepsilon} \, \mathrm{d}\Omega + \sum_{\mathbf{x}_K \in \Gamma_u} \mathbf{f}^{\mathrm{T}}(\mathbf{x}_K) \delta \mathbf{u}(\mathbf{x}_K) = \int_\Omega \mathbf{b}^{\mathrm{T}} \delta \mathbf{u} \, \mathrm{d}\Omega + \int_{\Gamma_t} \bar{\mathbf{t}}^{\mathrm{T}} \delta \mathbf{u} \, \mathrm{d}\Gamma \tag{34}$$

and

$$\sum_{\mathbf{x}_K \in \Gamma_u} \delta \mathbf{f}^{\mathrm{T}}(\mathbf{x}_K)[\mathbf{u}(\mathbf{x}_K) - \bar{\mathbf{u}}(\mathbf{x}_K)] = 0 \tag{35}$$

Note, Equation (34) is non-linear with respect to displacement $\mathbf{u}$, because of the non-linearity in the stress–strain relationship. From Equation (24), the MLS approximation of $\mathbf{u}(\mathbf{x}) = \{u_1(\mathbf{x}), u_2(\mathbf{x})\}^{\mathrm{T}}$ in two dimensions is

$$\mathbf{u}^h(\mathbf{x}) = \boldsymbol{\Phi}^{\mathrm{T}} \mathbf{d} \tag{36}$$

Copyright © 2003 John Wiley & Sons, Ltd.

where

$$\mathbf{\Phi}^{\mathrm{T}}(\mathbf{x}) = \begin{bmatrix} \Phi_1(\mathbf{x}) & 0 & \Phi_2(\mathbf{x}) & 0 & \cdots & \Phi_N(\mathbf{x}) & 0 \\ 0 & \Phi_1(\mathbf{x}) & 0 & \Phi_2(\mathbf{x}) & \cdots & 0 & \Phi_N(\mathbf{x}) \end{bmatrix} \tag{37}$$

$\mathbf{d} = \{d_1^1, d_1^2, \ldots, d_N^1, d_N^2\}^{\mathrm{T}} \in \Re^{2N}$ is the vector of nodal parameters or generalized displacements, and N is the total number of nodal points in Ω. Applying the MLS approximation of Equation (36) into Equations (34) and (35) yields a system of non-linear algebraic equations, which must be solved by iterative methods. The standard Newton–Raphson method was used to solve these non-linear equations, as follows.

Let $\mathbf{d}^r$ denote the nodal parameter vector at the r-th iteration. Upon Taylor series expansion at $\mathbf{d}^r$ and retaining only the linear term, Equations (34) and (35) leads to

$$\begin{bmatrix} \mathbf{k}(\mathbf{d}^r) & \mathbf{G} \\ \mathbf{G}^{\mathrm{T}} & \mathbf{0} \end{bmatrix} \begin{Bmatrix} \Delta\mathbf{d}^r \\ \mathbf{f}_R \end{Bmatrix} - \begin{Bmatrix} \mathbf{f}^{\mathrm{ext}} - \mathbf{f}^{\mathrm{int}}(\mathbf{d}^r) \\ \mathbf{g} - \mathbf{h}(\mathbf{d}^r) \end{Bmatrix} = \mathbf{0} \tag{38}$$

where $\Delta\mathbf{d}^r = \mathbf{d}^{r+1} - \mathbf{d}^r$ is the incremental solution, $\mathbf{h}(\mathbf{d}^r) = \{\mathbf{\Phi}^{\mathrm{T}}(\mathbf{x}_{K_1})\mathbf{d}^r, \ldots, \mathbf{\Phi}^{\mathrm{T}}(\mathbf{x}_{K_L})\mathbf{d}^r\}^{\mathrm{T}} \in \Re^{2L}$,

$$\mathbf{k} = [\mathbf{k}_{IJ}^r] = \begin{bmatrix} \mathbf{k}_{11}^r & \mathbf{k}_{12}^r & \cdots & \mathbf{k}_{1N}^r \\ \mathbf{k}_{21}^r & \mathbf{k}_{22}^r & \cdots & \mathbf{k}_{2N}^r \\ \vdots & \vdots & \vdots & \vdots \\ \mathbf{k}_{N1}^r & \mathbf{k}_{N2}^r & \cdots & \mathbf{k}_{NN}^r \end{bmatrix} \in \mathscr{L}(\Re^{2N} \times \Re^{2N}) \tag{39}$$

is the tangent stiffness matrix at $\mathbf{d}^r$ with

$$\mathbf{k}_{IJ}^r = \int_\Omega \mathbf{B}_I^{\mathrm{T}} \left[\frac{\partial\boldsymbol{\varepsilon}}{\partial\boldsymbol{\sigma}}\bigg|_{\mathbf{d}_r} \right]^{-1} \mathbf{B}_J \, \mathrm{d}\Omega \in \mathscr{L}(\Re^2 \times \Re^2) \tag{40}$$

$$\mathbf{G}^{\mathrm{T}} = \begin{bmatrix} \Phi_1(\mathbf{x}_1) & 0 & \Phi_1(\mathbf{x}_2) & 0 & \cdots & \Phi_1(\mathbf{x}_N) & 0 \\ 0 & \Phi_1(\mathbf{x}_1) & 0 & \Phi_1(\mathbf{x}_2) & \cdots & 0 & \Phi_1(\mathbf{x}_N) \\ \Phi_2(\mathbf{x}_1) & 0 & \Phi_2(\mathbf{x}_2) & 0 & \ldots & \Phi_2(\mathbf{x}_N) & 0 \\ \cdots & \Phi_2(\mathbf{x}_1) & 0 & \Phi_2(\mathbf{x}_2) & \ldots & 0 & \Phi_2(\mathbf{x}_N) \\ \vdots & \vdots & \vdots & \vdots & \vdots & \vdots & \vdots \\ \Phi_L(\mathbf{x}_1) & 0 & \Phi_L(\mathbf{x}_2) & 0 & \ldots & \Phi_L(\mathbf{x}_N) & 0 \\ 0 & \Phi_L(\mathbf{x}_1) & 0 & \Phi_L(\mathbf{x}_2) & \ldots & 0 & \Phi_L(\mathbf{x}_N) \end{bmatrix}$$

$$\in \mathscr{L}(\Re^{2L} \times \Re^{2N}) \tag{41}$$

is a matrix comprising shape functions of L nodes at which the displacement boundary conditions are prescribed on Γ_u, $\mathbf{f}_R = \{f_1(\mathbf{x}_{K_1}), f_2(\mathbf{x}_{K_1}), \ldots, f_1(\mathbf{x}_{K_L}), f_2(\mathbf{x}_{K_L})\}^{\mathrm{T}} \in \Re^{2L}$ is the vector

Copyright © 2003 John Wiley & Sons, Ltd.

of all reaction forces on Γ_u,

$$\mathbf{f}^{\text{ext}} = \int_{\Omega} \mathbf{\Phi}^{\mathrm{T}} \mathbf{b}\, \mathrm{d}\Omega + \int_{\Gamma_i} \mathbf{\Phi}^{\mathrm{T}} \bar{\mathbf{t}}\, \mathrm{d}\Gamma \in \Re^{2N} \tag{42}$$

is the external force vector. Noting that $\mathbf{d}_J^r = \{d_{J1}^r, d_{J2}^r\}^{\mathrm{T}} \in \Re^2$, $\mathbf{f}^{\text{int}}(\mathbf{d}^r) = \{\mathbf{f}_1^{\text{int}}(\mathbf{d}^r), \ldots, \mathbf{f}_N^{\text{int}}(\mathbf{d}^r)\}^{\mathrm{T}} \in \Re^{2N}$ is the internal force vector with

$$\mathbf{f}_I^{\text{int}}(\mathbf{d}^r) = \int_{\Omega} \mathbf{B}_I^{\mathrm{T}} \left[\left. \frac{\partial \boldsymbol{\varepsilon}}{\partial \boldsymbol{\sigma}} \right|_{\mathbf{d}_r} \right]^{-1} \mathbf{B}_J \mathbf{d}_J^r\, \mathrm{d}\Omega \in \Re^2 \tag{43}$$

and

$$\mathbf{B}_I = \begin{bmatrix} \Phi_{I,1} & 0 \\ 0 & \Phi_{I,2} \\ \Phi_{I,2} & \Phi_{I,1} \end{bmatrix} \tag{44}$$

Equation (38) represents a system of linear equations in $\Delta\mathbf{d}^r$ and can be easily solved using standard numerical methods. Hence, the total solution at the $(r+1)$th iteration is

$$\mathbf{d}^{r+1} = \mathbf{d}^r + \Delta\mathbf{d}^r \tag{45}$$

The iteration in Equation (45) is continued until both convergence criteria, defined by

$$\left\| \frac{\Delta\mathbf{d}^r}{\mathbf{d}^{r+1}} \right\| \leqslant \varepsilon_1 \tag{46}$$

and

$$\left\| \frac{\Delta\mathbf{R}^r}{\mathbf{R}^{r+1}} \right\| \leqslant \varepsilon_2 \tag{47}$$

are satisfied, where $\mathbf{R}^r = \mathbf{f}^{\text{ext}} - \mathbf{f}^{\text{int}}(\mathbf{d}^r)$ is the residual at the i-th iteration, $\Delta\mathbf{R}^r = \mathbf{R}^{r+1} - \mathbf{R}^r$, and ε_1 and ε_2 are the pre-selected tolerances.

To perform numerical integration in Equations (40), (42) and (43), a background mesh is required, which can be independent of the arrangement of the meshless nodes. However, in this study, the nodes of the background mesh coincide with the meshless nodes. Standard Gaussian quadratures were used to evaluate the integrals for assembling the stiffness matrix and the force vector. In general, a 4×4 quadrature is adequate, except in the cells surrounding a high stress gradient (e.g. near a crack tip) where a 8×8 quadrature is suggested.

In solving for $\Delta\mathbf{d}^r$, the essential boundary conditions must be enforced. The lack of Kronecker delta properties in the meshless shape functions presents some difficulty in imposing the essential boundary conditions in EFGM. Nevertheless, several methods are currently available for enforcing essential boundary conditions. A full transformation method [12, 25] was used in this work.

It should be noted that the generalized displacement vector $\mathbf{d}$ represents the nodal parameters, not the actual displacements at the meshless nodes. However, the actual displacement

Copyright © 2003 John Wiley & Sons, Ltd.

vector $\hat{\mathbf{d}} = \{\mathbf{u}(\mathbf{x}_1), \ldots, \mathbf{u}(\mathbf{x}_N)\}^{\mathrm{T}} \in \Re^{2N}$ can be easily calculated from

$$\hat{\mathbf{d}} = \mathbf{\Lambda}\mathbf{d} \tag{48}$$

where $\mathbf{\Lambda} = [\mathbf{\Phi}(\mathbf{x}_1), \ldots, \mathbf{\Phi}(\mathbf{x}_N)]^{\mathrm{T}} \in \mathscr{L}(\Re^{2N} \times \Re^{2N})$ is the transformation matrix.

5. NUMERICAL EXAMPLES

5.1. Example 1: Crack-tip fields by boundary layer analysis

In order to evaluate the accuracy of predicted crack-tip fields, the near-tip region of a mode I plane stress crack in a semi-circular patch of homogeneous elastic–plastic material, shown in Figure 4(a), was investigated. The near-tip fields are supposed to be dominated by the well-known HRR solution in Equations (7)–(9). The patch had a radius $R = 800$ units and was discretized with 253 meshless nodes, as shown in Figure 4(b). The weight function parameter $\beta = 3$ was used for meshless analysis. The domain of the patch was divided into 240 cells with corner points coincident with the 253 meshless nodes, for the purposes of numerical integration. A boundary layer approach within the framework of small deformation was employed to calculate the near-tip elastic–plastic fields by imposing mode I linear-elastic displacement field on the circular boundary remote from the crack tip and homogenous boundary conditions $[u_2(r, 0) = 0]$ ahead of the crack. The material parameters were selected as follows: $E = 209,400$ units, $\nu = 0.3$, $\sigma_0 = 698$ units, $\alpha = 0.1$, and $n = 3$. A plane stress condition was employed.

Figures 5(a) and 5(b) present the variations of the normalized stress components σ_r/σ_0, σ_θ/σ_0, and $\tau_{r\theta}/\sigma_0$ from the present meshless analysis using Types I and II enriched bases, respectively, as functions of normalized radial distance $r\sigma_0/J$, for $\theta = 41.3°$. For comparisons, both HRR (Equation (7)) and LEFM solutions are also plotted in Figures 5(a) and 5(b). When $r \to 0$, the plastic strain is much larger than the elastic strain and hence, the stress field obtained by the proposed meshless method matches with the HRR field. As r becomes larger, the elastic strain dominates over the plastic strain. Therefore, the associated stress field from the meshless analysis is well described by the LEFM solution. Similar comparisons of meshless results for $\theta = 86.3°$ and $131.3°$, shown in Figures 6 and 7, also indicate excellent agreement with the HRR or LEFM solutions.

In summary, the numerical results obtained by the meshless method using proposed basis functions correlate very well with the theoretical solution in the whole region considered, whether for the near-tip asymptotic field or for the far-tip elastic field. This demonstrates the high accuracy of the proposed method in solving elastic–plastic crack problems.

5.2. Example 2: J-integral evaluations for SE(T), DE(T), and $M(T)$ specimens

Consider three rectangular plates illustrated in Figures 8(a)–(c), comprising single-edge tension [SE(T)], double-edge tension [DE(T)], and middle tension [$M(T)$] specimens [26], subjected to a far-field remote tensile stress σ^∞. For numerical analysis, values of width $2W = 1.016$m, length $2L = 5.08$m, crack length $a = 0.254$m. The material parameters involved: $E = 206.8$ GPa, $\nu = 0.3$, $\sigma_0 = 154.8$ MPa, $\alpha = 3.8$, and $n = 8.073$.

Copyright © 2003 John Wiley & Sons, Ltd.

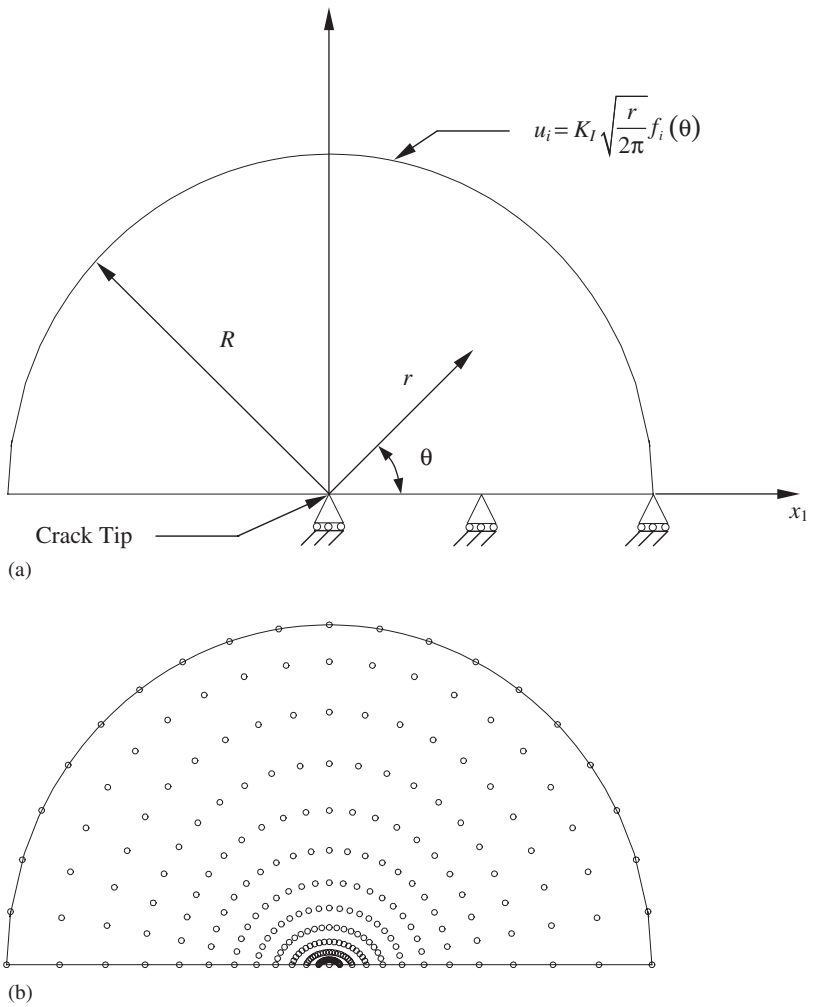

Figure 4. Boundary layer analysis: (a) semi-circular patch of radius; and (b) meshless discretization (253 nodes).

Due to symmetry, meshless discretizations were performed for only half the plate for the SE(T) specimen, and a quarter of the plate for the DE(T) and $M(T)$ specimens, as depicted by the shaded regions in Figures 8(a)–8(c). The discretization involves 286 regularly distributed nodes, however, in the vicinity of the crack-tip region $Q_1Q_2Q_3Q_4$, [see Figure 9(a)] additional 63 nodes were used, as shown in the Figure 9(b), for a total of 349 meshless nodes. A domain of size $2b \times b$, with $b = 0.254$ m, was used to calculate the J-integral. The domain of the plate in Figure 9(a) was divided by 10×25 rectangular cells with corner points coincident with the 286 meshless nodes, solely for the purpose of numerical integration. An 8×8 Gaussian integration scheme was employed over the background grid. The weight function parameter

Copyright © 2003 John Wiley & Sons, Ltd.

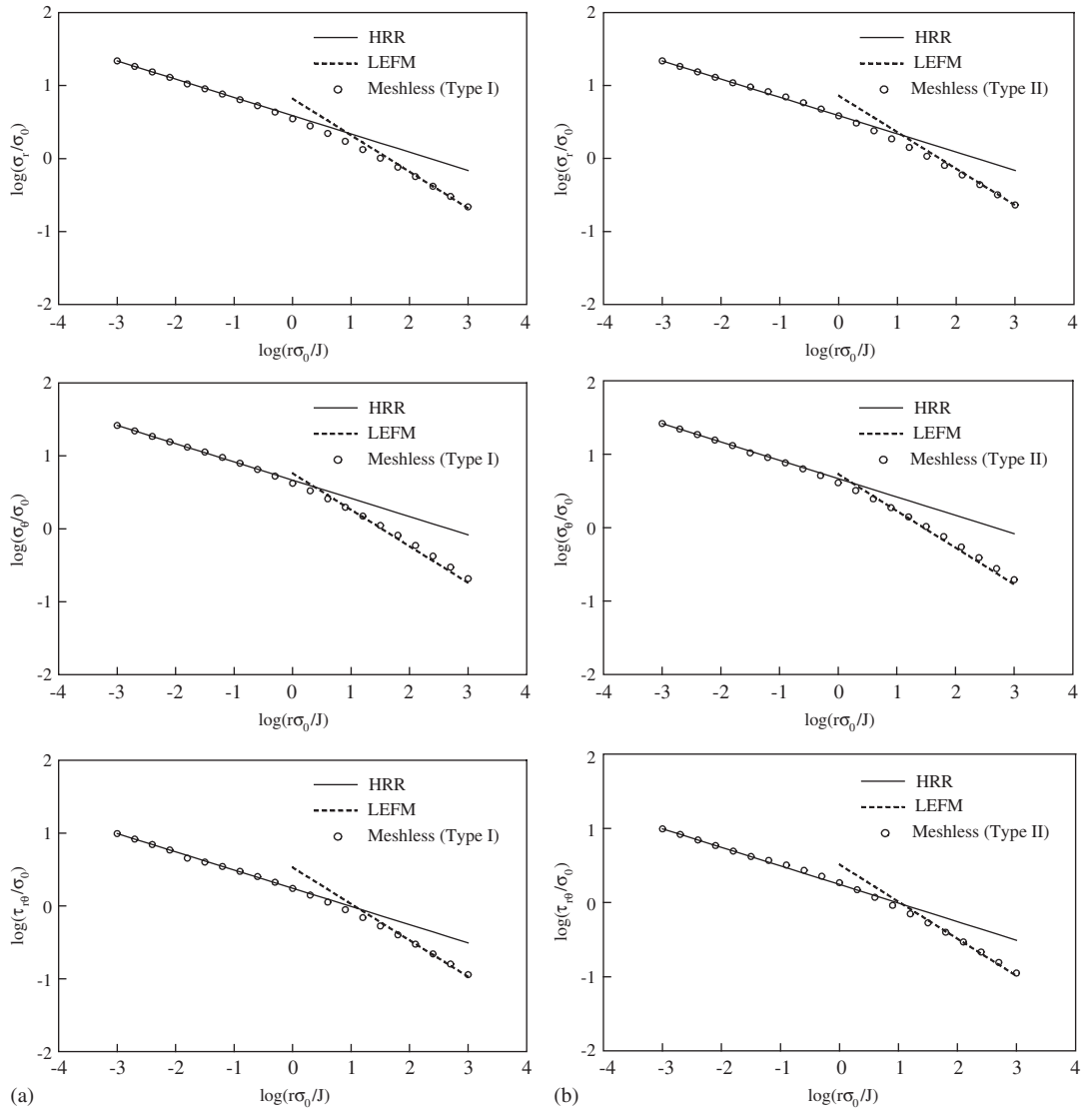

Figure 5. Crack-tip stress components along radial lines for $\theta = 41.3^{\circ}$: (a) Type I enriched basis; and (b) Type II enriched basis.

$\beta = 3$ was used for meshless analysis. Both plane stress and plane strain conditions were employed.

Figures 10(a)–(c) show plots of J-integral vs σ^{∞} for the plane stress condition, as predicted by the meshless method for SE(T), DE(T), and $M(T)$ plates, respectively using both Types I and II basis functions. A domain form of Equation (1) was used in calculating the J-integral [12]. Also plotted in the same figures are the corresponding analytical J-integral solutions,

Copyright © 2003 John Wiley & Sons, Ltd.

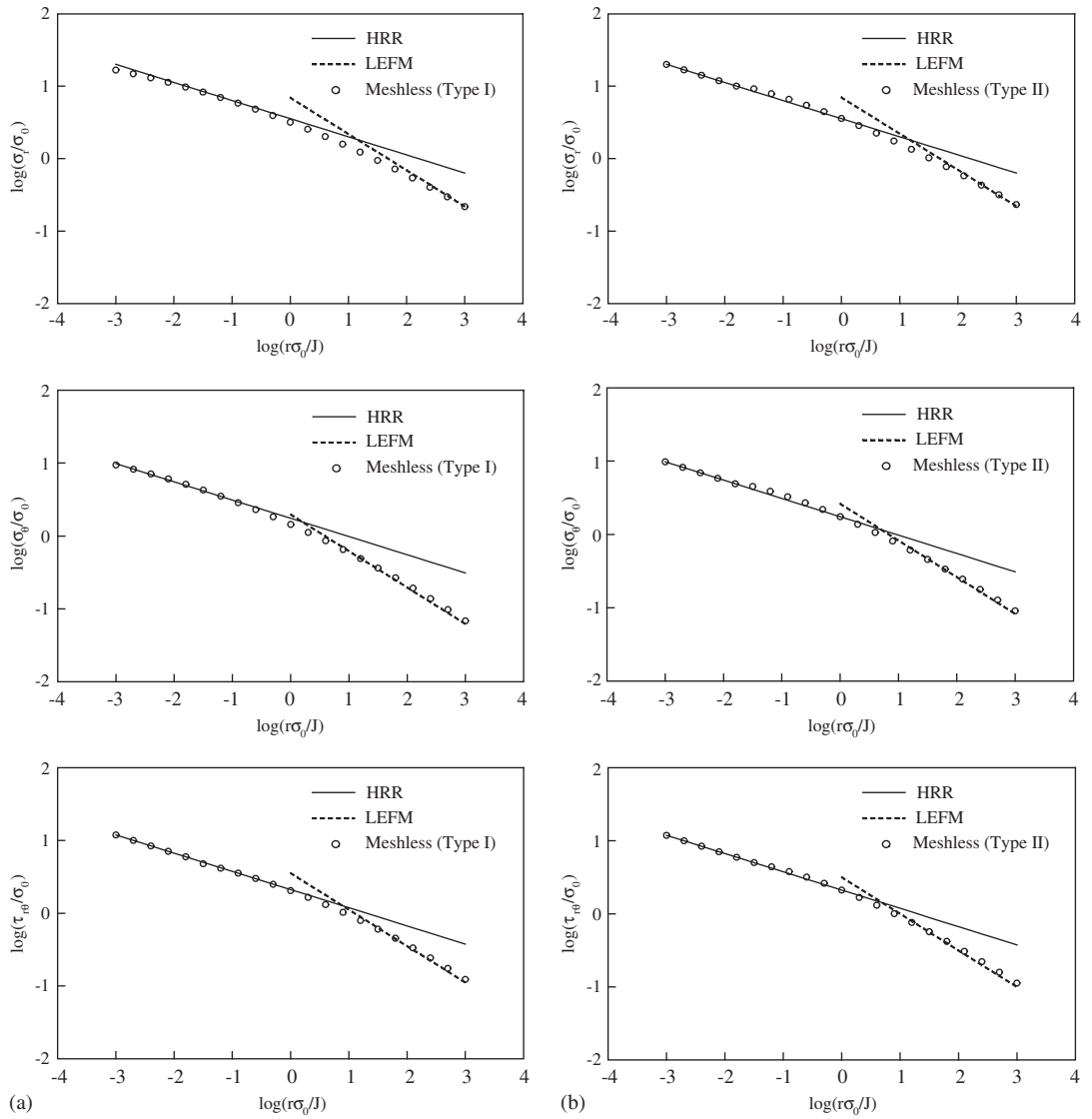

Figure 6. Crack-tip stress components along radial lines for $\theta = 86.3^\circ$: (a) Type I enriched basis; and (b) Type II enriched basis.

which are described in Appendix A. Similar comparisons between meshless and analytical results are shown in Figure 11(a)–(c) for the plane strain condition. In both stress states, the meshless results using proposed basis functions match very well with the analytical solutions for load intensities and material constants considered.

Copyright © 2003 John Wiley & Sons, Ltd.

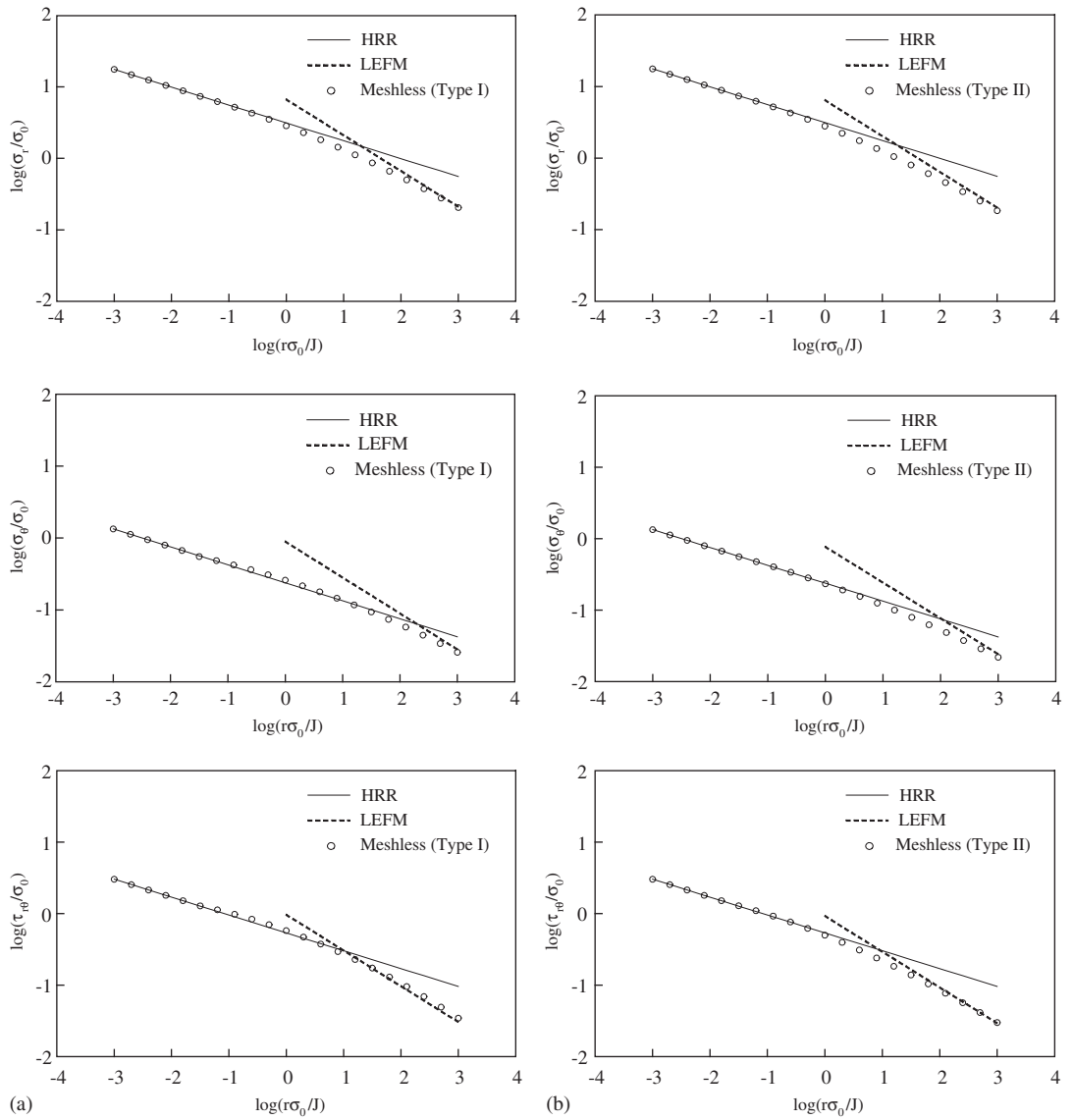

Figure 7. Crack-tip stress components along radial lines for $\theta = 131.3^{\circ}$: (a) Type I enriched basis; and (b) Type II enriched basis.

5.3. Example 3: Crack-mouth opening displacement evaluation for three point bend specimen specimens

Consider a three-point bend specimen with length $L = 5.08$m, depth $H = 0.508$m, and thickness $t = 1$ mm, as shown in Figure 12(a). A concentrated load $P = 1420$ N was applied at the middle of the beam of span $L_S = 4.572$ m and two supports were symmetrically placed with

Copyright © 2003 John Wiley & Sons, Ltd.

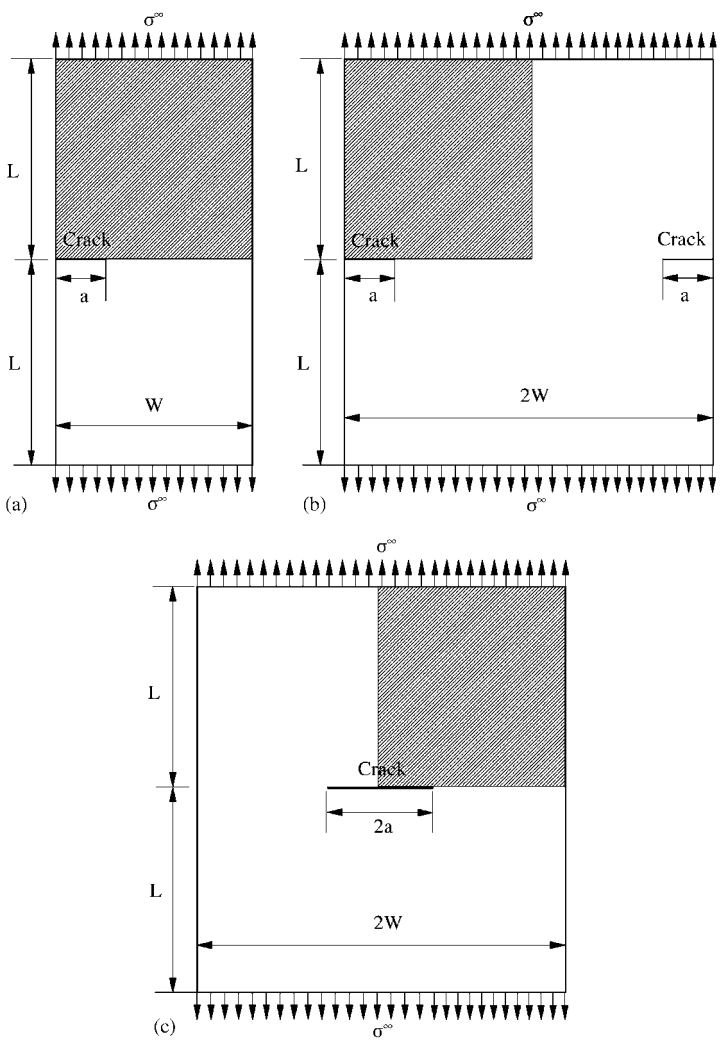

Figure 8. Fracture specimens under far-field tension: (a) SE(T) specimen; (b) DE(T) specimen; and (c) $M(T)$ specimen.

respect to an edge crack of length a. The material parameters involved: $E = 207\,\text{GPa}$, $v = 0.3$, $\sigma_0 = 154.8\,\text{MPa}$, $\alpha = 3.8$, and $n = 8.073$. A plane stress condition was assumed.

Due to symmetric geometry and loading with respect to the crack, only a half model of the beam, as shown in Figure 12(b), was analysed. Figure 13(a) shows the details of the meshless discretization involving 286 regularly distributed nodes, and additional 63 nodes in the vicinity of the crack-tip region for a total of 349 meshless nodes. The domain of the plate in Figure 12(a) was divided by 10×25 rectangular cells with corner points coincident with the 286 meshless nodes, solely for the purpose of numerical integration. An 8×8 Gaussian

Copyright © 2003 John Wiley & Sons, Ltd.

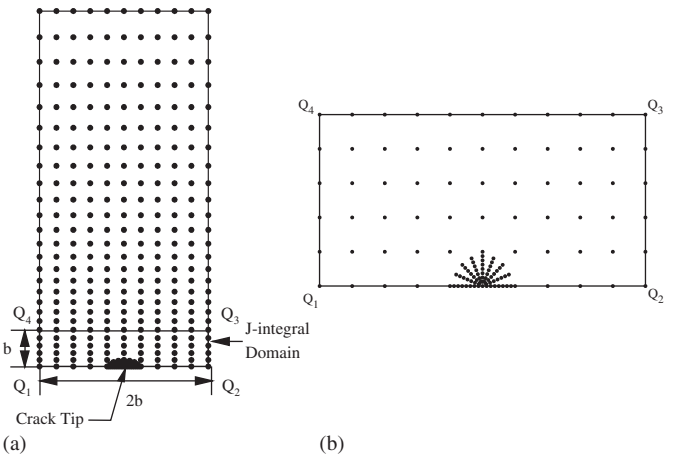

Figure 9. Meshless discretization of fracture specimens: (a) half (SE(T)) and Quarter (DE(T) and $M(T)$) model; and (b) closeup of $Q_1Q_2Q_3Q_4$ region.

integration scheme was employed over the background grid. The weight function parameter $\beta = 3$ was used for meshless analysis. For the purpose of comparison elastic–plastic finite element analysis using ABAQUS (Version 6.2) [27] was also performed on the half model of the beam as shown in Figure 12(b). Figure 13(b) depicts the finite element mesh for the half model of the beam. Second-order elements from ABAQUS (Version 6.2) element library were used. The element type was CPS8—the reduced integration, eight-noded quadrilateral element. The number of elements and nodes were 410 and 1273, respectively. Focused elements with collapsed nodes were employed in the vicinity of crack tip. A 2×2 Gaussian integration was employed.

Figure 14 shows a plot of crack-mouth opening displacement (δ) vs load (P), as predicted by the meshless method using both Type I or Type II basis functions. However, both basis functions led to very close results, which are practically coincident with each other. Also plotted in the same figures are the corresponding finite element results. The meshless results using proposed basis functions are in good agreement with the finite element solutions, indicating that the new basis functions are capable of predicting elastic–plastic deformations of cracked structures accurately.

5.4. Example 4: Comparison with experimental data from blunt-notch specimen

In this example, the ability of the meshless method in modelling elastic–plastic deformations at a stress concentration is demonstrated. The meshless results are compared with experimental results of a blunt-notch specimen tested by Newman *et al.* [28]. The blunt-notch specimen, shown in Figure 15, is similar to the $M(T)$ specimen, except that a small hole was drilled at the end of the saw cut, and the holes were polished to help prevent premature fracture. The specimen was made of 2024-T3 aluminium with elastic modulus $E = 10400$ ksi and Poisson's ratio $v = 0.3$. Due to symmetry, a meshless discretization involving 615 nodes was employed for a quarter of the blunt-notch specimen, as depicted in Figure 16. The geometric

Copyright © 2003 John Wiley & Sons, Ltd.

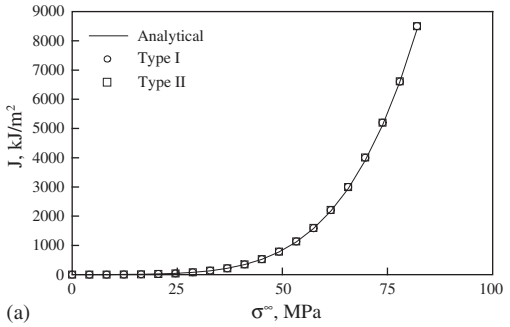

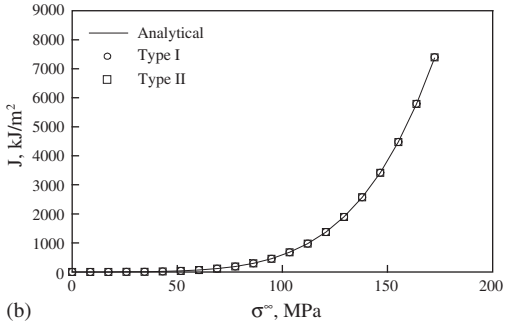

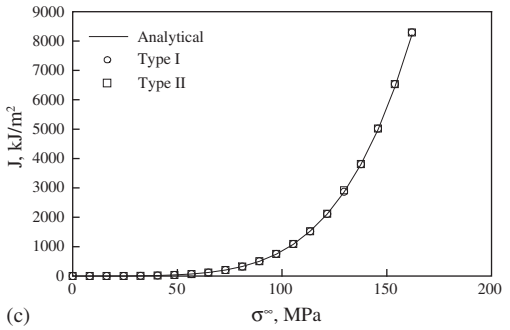

Figure 10. J-Integral vs σ^{∞} for all the three specimens under plane stress: (a) SE(T) specimen; (b) DE(T) specimen; and (c) $M(T)$ specimen.

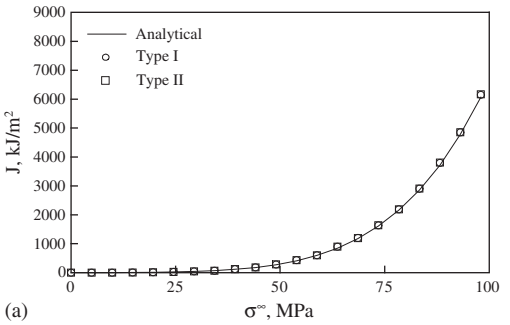

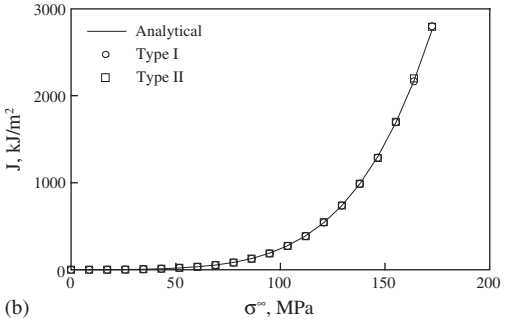

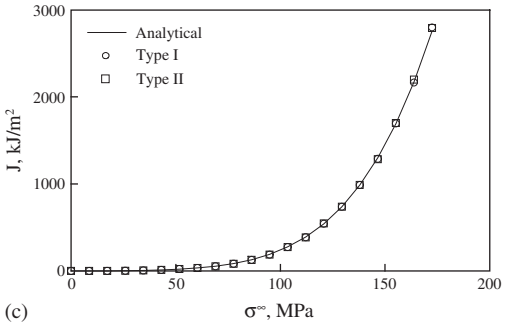

Figure 11. J-Integral vs σ^{∞} for all the three specimens under plane strain: (a) SE(T) specimen; (b) DE(T) specimen; and (c) $M(T)$ specimen.

parameters are as follows: $h = 6$ in, $W = 5$ in, and $c/W = 1/3$. A far-field remote tensile stress $\sigma^{\infty} = 35$ MPa was applied along the top edge of the model. Figure 17 shows the stress–strain data of 2024-T3 aluminium obtained from Reference [27]. By fitting these raw data by the Ramberg–Osgood equation (Equation (3)), also shown in Figure 17, the following material parameters were estimated: $\sigma_0 = 50$ ksi, $\alpha = 0.453$, and $n = 12.37$.

Figure 18 compares the applied stress vs notch-root displacement relationship predicted by the meshless method with the experimental record [28]. The notch-root displacement, V_2 is defined as the displacement measured at both notch roots during monotonic loading to failure

Copyright © 2003 John Wiley & Sons, Ltd.

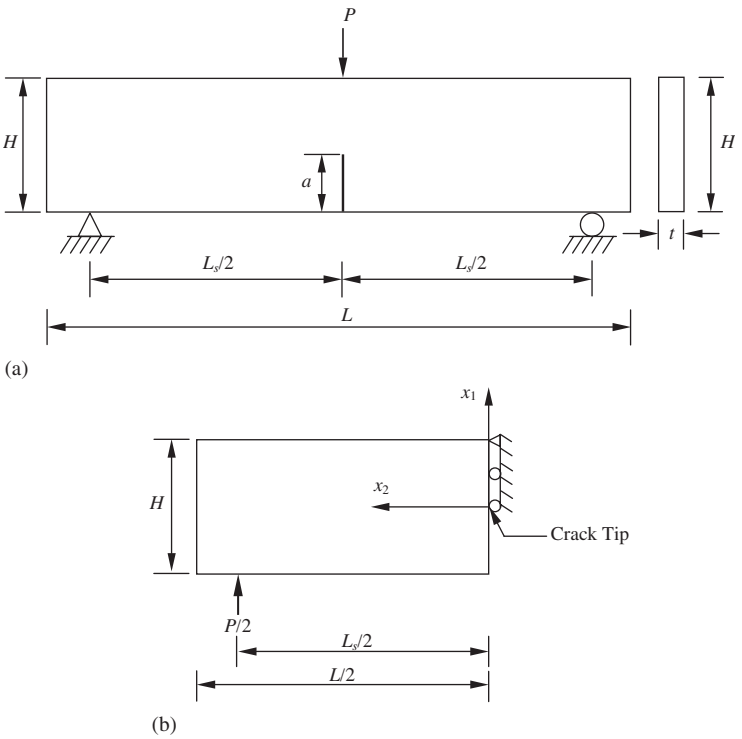

Figure 12. Three-point bend specimen under mode I loading: (a) Geometry and loads; and (b) half model.

and is also shown in Figure 18. According to Figure 18, the meshless results using either Type I or Type II basis show excellent agreement with the experimental measurements, indicating that the new basis functions are also capable of capturing elastic–plastic deformations at a stress concentration effectively.

The CPU time required for meshless methods increases with the length of basis functions, because the dimension of the matrix that needs to be inverted for the construction of meshless shape function is directly proportional to the square of the length of basis function. Hence, the CPU time using the Type II enriched basis is slightly higher than that using the Type I enriched basis. All numerical examples of this study show that in terms of accuracy, the performance of the Type I enriched basis function is comparable to the Type II enriched basis function.

6. CONCLUSIONS

An enriched meshless method is presented for fracture analysis of cracks in homogeneous, isotropic, non-linear-elastic, two-dimensional solids, subject to mode-I loading conditions. The method involves an element-free Galerkin formulation and two new enriched basis functions (Types I and II) to capture the Hutchinson–Rice–Rosengren singularity field in non-linear

Copyright © 2003 John Wiley & Sons, Ltd.

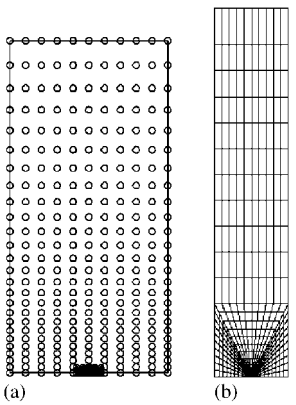

Figure 13. Three-point bend specimen under mode I loading: (a) meshless discretization of half model (231 nodes); and (b) finite element discretization of half model (410 Elements and 1237 Nodes).

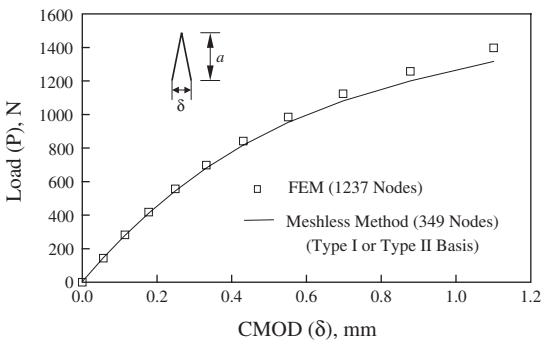

Figure 14. Comparison of crack-mouth opening displacement predicted by the meshless method with finite element results.

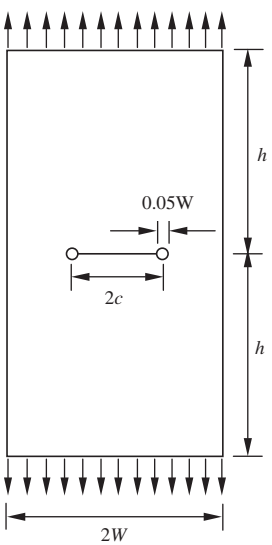

Figure 15. Geometry of the blunt-notch specimen.

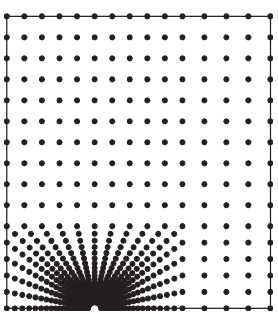

Figure 16. Meshless discretization using 615 nodes (1/4 model).

fracture mechanics. The Type I enriched basis function can be viewed as a generalized enriched basis function, which degenerates to the linear-elastic basis function when the material hardening exponent is unity. The Type II enriched basis function entails further improvements of the Type I basis function by adding trigonometric functions. Four numerical examples are presented to illustrate the proposed method. The boundary layer analysis indicates that the

Copyright © 2003 John Wiley & Sons, Ltd.

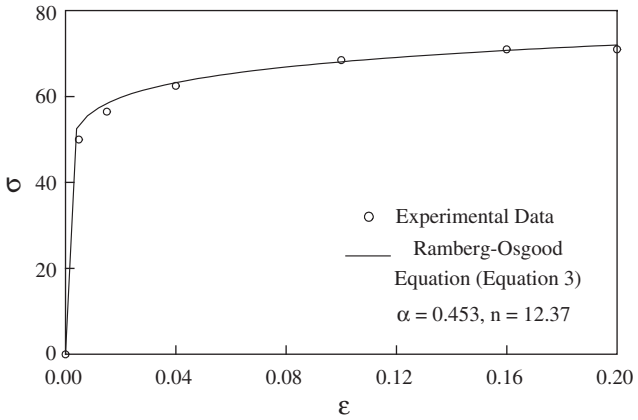

Figure 17. Stress–strain curve of 2024-T3 aluminium.

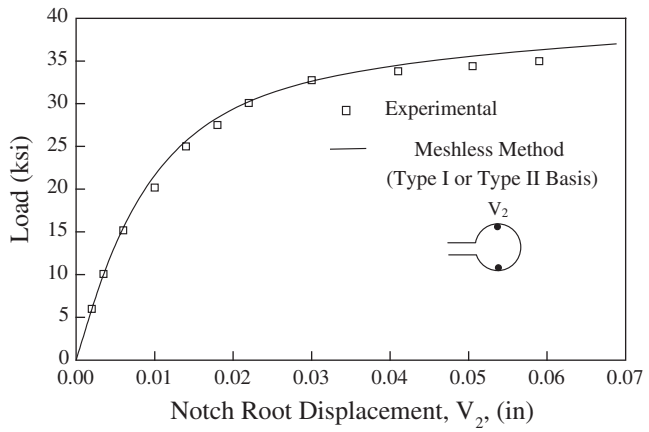

Figure 18. Comparison of notch-root displacement predicted by the meshless method with experimental results.

crack-tip field predicted by using the proposed basis functions matches with the theoretical solution very well in the whole region considered, whether for the near-tip asymptotic field or for the far-tip elastic field. This demonstrates the high accuracy of the proposed method in solving elastic–plastic crack problems. Numerical analyses of standard fracture specimens by the proposed meshless method also yield accurate estimates of the J-integral for the applied load intensities and material properties considered. Also, the crack-mouth opening displacement evaluated by the proposed meshless method is in good agreement with elastic–plastic finite element results. Furthermore, the meshless results show excellent agreement with the experimental measurements, indicating that the new basis functions are also capable of capturing elastic–plastic deformations at a stress concentration effectively.

Copyright © 2003 John Wiley & Sons, Ltd.

APPENDIX A: J-INTEGRAL FOR SE(T), DE(T), AND M(T) SPECIMENS

Consider SE(T), DE(T), and $M(T)$ specimens subjected to quasi-static far-field tension stress σ^{∞}. The geometrical parameters of these specimens are defined in Figures 8(a)–8(c). The total J-integral can be obtained from

$$J = J_e + J_p \tag{A1}$$

where J_e and J_p are the elastic and plastic solutions, respectively, and are defined as follows.

A.1. SE(T) *specimen* [26]

The elastic J is

$$J_e = \frac{\sigma^{\infty^2}\pi a}{E'}[0.265(1-a/W)^4 + (0.857 + 0.265a/W)/(1-a/W)^{1.5}]^2 \tag{A2}$$

The plastic J is

$$J_p = \frac{\alpha\sigma_0^2}{E}(W-a)h_1(a/W,n)\left(\frac{P}{P_0}\right)^{n+1} \tag{A3}$$

where $P = \sigma^{\infty} WB$ is the far-field tensile load,

$$P_0 = \begin{cases} 1.072\eta B(a-W)\sigma_0, & \text{plane stress} \\ 1.455\eta B(a-W)\sigma_0, & \text{plane strain} \end{cases} \tag{A4}$$

is the reference load, and $h_1(a/W,n)$ is a dimensionless plastic influence function that are tabulated in Reference [26].

A.2. DE(T) *specimen* [26]

The elastic J is

$$J_e = \frac{\sigma^{\infty^2}\pi a}{E'}[1.12 + 0.2(a/W) - 1.2(a/W)^2 + 1.93(a/W)^3]^2 \tag{A5}$$

The plastic J is

$$J_p = \frac{\alpha\sigma_0^2}{E}(W-a)h_1(a/W,n)\left(\frac{P}{P_0}\right)^{n+1} \tag{A6}$$

where $P = \sigma^{\infty} 2WB$ is the far-field tensile load,

$$P_0 = \begin{cases} \dfrac{4}{\sqrt{3}}\sigma_0(W-a)B, & \text{plane stress} \\ \left[0.72 + 1.82\left(1 - \dfrac{a}{W}\right)\right]\sigma_0 WB, & \text{plane strain} \end{cases} \tag{A7}$$

is the reference load, and $h_1(a/W,n)$ is a dimensionless plastic influence function that are tabulated in Reference [26].

Copyright © 2003 John Wiley & Sons, Ltd.

A.3. M(T) specimen [26]

The elastic J is

$$J_e = \frac{\sigma^{\infty^2}\pi a}{E'}[1 + 0.128a/W - 0.288(a/W)^2 + 1.525(a/W)^3]^2 \tag{A8}$$

The plastic J is

$$J_p = \frac{\alpha\sigma_0^2}{E}(W - a)h_1(a/W, n)\left(\frac{P}{P_0}\right)^{n+1} \tag{A9}$$

where $P = \sigma^\infty 2WB$ is the far-field tensile load,

$$P_0 = \begin{cases} 2B(a - W)\sigma_0, & \text{plane stress} \\ \dfrac{4}{\sqrt{3}}B(a - W)\sigma_0, & \text{plane strain} \end{cases} \tag{A10}$$

is the reference load, and $h_1(a/W, n)$ is a dimensionless plastic influence function that are tabulated in Reference [26].

In Equations (A2), (A5), and (A8),

$$E' = \begin{cases} E, & \text{plane stress} \\ \dfrac{E}{1 - \nu^2}, & \text{plane strain} \end{cases} \tag{A11}$$

is the effective modulus of elasticity and ν is the Poisson ratio.

ACKNOWLEDGEMENTS

The authors acknowledge the financial support of the U.S. National Science Foundation (NSF) under Award No. CMS-9900196. The NSF program director was Dr Ken Chong.

REFERENCES

1. Irwin GR. Analysis of stress and strain near the end of a crack traversing a plate. *Journal of Applied Mechanics* 1957; **24**(3):361–364.
2. Hutchinson JW. Singular behavior at the end of a tensile crack in a hardening material. *Journal of Mechanics and Physics of Solids* 1968; **16**:13–31.
3. Rice JR, Rosengren GF. Plane strain deformation near a crack tip in a power hardening material. *Journal of Mechanics and Physics of Solids* 1968; **16**:1–13.
4. Eshelby JD. The continuum theory of lattice defects. *Solid State Physics*, vol. 3. Academic Press: New York, 1956; 79–144.
5. Cherepanov GP. Crack propagation in continuous media. *Applied Mathematics and Mechanics* 1967; **31**(3): 467–488.
6. Rice JR. A path independent integral and the approximate analysis of strain concentrations by notches and cracks. *Journal of Applied Mechanics* 1968; **35**:379–386.
7. Belytschko T, Lu YY, Gu L. Crack propagation by element-free Galerkin Methods. *Engineering Fracture Mechanics* 1995; **51**(2):295–315.
8. Belytschko T, Tabbara M. Dynamic fracture using element-free Galerkin methods. *International Journal for Numerical Methods in Engineering* 1996; **39**:923–938.
9. Fleming M, Chu YA, Moran B, Belytschko T, Lu YY, Gu L. Enriched Element-free Galerkin methods for crack-tip fields. *International Journal for Numerical Methods in Engineering* 1997; **40**:1483–1504.

Copyright © 2003 John Wiley & Sons, Ltd.

10. Sukumar N, Moran B, Belytschko T. The natural element method in solid mechanics. *International Journal for Numerical Methods in Engineering* 1998; **43**:839–887.
11. Kaljevic I, Saigal S. An improved element free Galerkin formulation. *International Journal for Numerical Methods in Engineering* 1997; **40**:2953–2974.
12. Rao BN, Rahman S. An efficient meshless method for fracture analysis of cracks. *Computational Mechanics* 2000; **26**:398–408.
13. Rao BN, Rahman S. A coupled meshless-finite element method for fracture analysis of cracks. *International Journal of Pressure Vessels and Piping* 2001; **78**(9):647–657.
14. Rao BN, Rahman S. Probabilistic fracture mechanics by Galerkin meshless methods—Part I: Rates of stress-intensity factors. *Computational Mechanics* 2002; **28**(5):351–364.
15. Rahman S, Rao BN. Probabilistic fracture mechanics by Galerkin meshless methods—Part II: Reliability analysis. *Computational Mechanics* 2002; **28**(5):365–374.
16. Rao BN, Rahman S. Meshfree analysis of cracks in isotropic functionally graded materials. *Engineering Fracture Mechanics* 2003; **70**(1):1–27.
17. Xu Y, Saigal S. Element free Galerkin study of steady quasi-static crack growth in plane strain tension in elastic–plastic materials. *Computational Mechanics* 1998; **22**:255–265.
18. Pan J, Shih CF. Elastic–plastic analysis of combined mode I, II and III crack-tip fields under small-scale yielding conditions. *International Journal of Solids and Structures* 1992; **29**:2795–2814.
19. Betegon C, Hancock JW. Two-parameter characterization of elastic–plastic crack fields. *Journal of Applied Mech*anics 1991; **58**:104–113.
20. Parks DM. Advances in characterization of elastic–plastic crack-tip fields. *Topics in Fracture and Fatigue*. Springer, New York, 1992.
21. O'Dowd NP, Shih CF. Family of crack-tip fields characterized by a triaxiality parameter: Part I—Structure of fields. *Journal of the Mechanics and Physics of Solids* 1991; **39**(8):989–1015.
22. O'Dowd NP, Shih CF. Family of crack-tip fields characterized by a triaxiality parameter: Part I—Fracture applications. *Journal of the Mechanics and Physics of Solids* 1992; **40**(8):939–963.
23. Shih CF. Tables of Hutchinson–Rice–Rosengren singular field quantities. *MRL E-147*, Materials Research Laboratory, Brown University, 1983.
24. Lancaster P, Salkauskas K. Surfaces generated by moving least squares methods. *Mathematics of Computation* 1981; **37**:141–158.
25. Chen JS, Wang HP. New boundary condition treatments in meshfree computation of contact problems. *Computer Methods in Applied Mechanics and Engineering* 2000; **187**(3–4):441–468.
26. Anderson TL. *Fracture Mechanics*: *Fundamentals and Applications*. CRC Press: Boca Raton, FL, 1991.
27. ABAQUS, *User's Guide and Theoretical Manual*, *Version 6.2*, Hibbit, Karlson, and Sorenson, Inc.: Pawtucket, RI, 2002.
28. Newman Jr JC, Dawicke DS, Bigelow CA. Finite–element analyses and fracture simulation in thin-sheet aluminum alloy. *NASA TM 107662, NASA Langley Research Center*, Hampton, VA, 1992.

Copyright © 2003 John Wiley & Sons, Ltd.